catalysts

MDPI

Article

$Co(OH)_2$ Nanoflowers Decorated α-$NiMoO_4$ Nanowires as a Bifunctional Electrocatalyst for Efficient Overall Water Splitting

Zhiying Xu [1], Minghui Hao [1], Xin Liu [2], Jingjing Ma [3], Liang Wang [1], Chunhu Li [1] and Wentai Wang [1,*]

[1] Key Laboratory of Marine Chemistry Theory and Technology, Ministry of Education, College of Chemistry and Chemical Engineering, Ocean University of China, Qingdao 266100, China
[2] Institute for New Energy Materials and Low-Carbon Technologies, Tianjin University of Technology, Tianjin 300384, China
[3] State Key Laboratory of High-Efficiency Utilization of Coal and Green Chemical Engineering, Ningxia University, Yinchuan 750021, China
* Correspondence: wangwentai@ouc.edu.cn

Abstract: The development of bifunctional electrocatalysts with high catalytic activity and cyclic stability is an effective method for electrocatalytic water splitting. Herein, a promising hydroxide/oxide $Co(OH)_2$/α-$NiMoO_4$ NWs/CC heterostructure with nanoflowers decorating the nanowires was fabricated on a carbon cloth (CC) substrate via hydrothermal and calcination methods. In contrast to one-dimensional nanomaterials, the interfaces of $Co(OH)_2$ nanoflowers and α-$NiMoO_4$ nanowires on CC provide more active sites for electrocatalytic reactions; therefore, they exhibit obviously enhanced electrocatalytic activities in overall water splitting. Specifically, the $Co(OH)_2$/α-$NiMoO_4$ NWs/CC electrodes exhibit an overpotential of 183.01 mV for hydrogen evolution reaction (HER) and of 170.26 mV for oxygen evolution reactions (OER) at the current density of 10 mA cm^{-2} in 1.0 M KOH. Moreover, the electrocatalytic oxygen evolution reaction (OER) activity of the $Co(OH)_2$/α-$NiMoO_4$ NWs/CC electrocatalyst was enhanced after long-term stability tests.

Keywords: electrocatalytic water splitting; hydrogen evolution reaction (HER); oxygen evolution reaction (OER); heterostructure; $Co(OH)_2$; α-$NiMoO_4$ nanowires

Citation: Xu, Z.; Hao, M.; Liu, X.; Ma, J.; Wang, L.; Li, C.; Wang, W. $Co(OH)_2$ Nanoflowers Decorated α-$NiMoO_4$ Nanowires as a Bifunctional Electrocatalyst for Efficient Overall Water Splitting. *Catalysts* **2022**, *12*, 1417. https://doi.org/10.3390/catal12111417

Academic Editors: Dezhi Han and Ning Han

Received: 6 October 2022
Accepted: 7 November 2022
Published: 11 November 2022

1. Introduction

With the over-consumption of traditional fossil fuels and the growing environmental and energy shortage problems, there is a huge demand for clean renewable energy [1–4]. Hydrogen (H_2), with its cleanliness, small molecular mass, and high calorific value, is considered to be one of the most promising energy sources to replace traditional fossil fuels and is sustainable and pollution-free [5–7]. Precious metals (such as Pt [8] and Pd [9]) and precious metal oxides (such as IrO_2 [10] and RuO_2 [11]) are excellent electrocatalysts for hydrogen and oxygen evolution reactions, but their high cost and scarce sources limit their wide application in electrochemical water splitting. The low-cost transition metal-based electrocatalysts with both hydrogen and oxygen evolution reaction functions have attracted great interest in research [12], such as transition metal phosphides [13], hydroxides [14], sulfides [15], carbides [16], and metal alloys [17] being examples. However, there are still some problems with transition metal-based catalysts, such as high oxygen evolution overpotential, poor stability, mismatching of hydrogen evolution/oxygen evolution reactivity, and low energy conversion efficiency [12,18–20]. Therefore, it is of great significance to develop a series of new transition metal-based electrocatalysts with high efficiency and bifunctional properties for hydrogen and oxygen evolution reactions.

Recently, binary metal oxides, such as $NiCo_2O_4$ [21,22], $CoMoO_4$ [23,24], $NiMoO_4$ [25,26], and Zn_2SnO_4 [27], have been reported to exhibit higher electrocatalytic properties than single-component oxides and are considered as the most promising cheap alternatives to Pt-group electron catalysts in alkaline environments due to their feasible oxidation states

and high electrical conductivity. However, most Ni-Mo oxides are only suitable for HER rather than OER [28]. It is worth noting that cobalt hydroxide ($Co(OH)_2$), a transition metal hydroxide, shows excellent OER performance due to its multivalent oxidation state ($Co^{+2/+3/+4}$), good corrosion resistance, excellent chemical activity, and high theoretical capacitance (3460 F g^{-1}) [29–32]. However, the poor electrical conductivity and its property of being easy to agglomerate seriously hinder its practical application [33,34]. In recent reports, carbon cloth (CC) is often used as a substrate for the in situ growth of various composites to fabricate self-supporting electrodes, as it has excellent mechanical strength, flexibility, and electrical conductivity [35–37]. The interwoven carbon fibers can also provide a larger usable surface than some planar substrates [36,38].

Structural design and surface engineering have been employed as effective strategies to improve the performance of electrochemical water splitting. Electrocatalysts with nanoflowers, nanowires, or macroporous morphologies can increase the specific surface area, expose more reactive active sites, and accelerate the diffusion of reactants/products and can therefore improve electrochemical performance. In addition, the construction of heterogeneous structures is an efficient interface engineering strategy that shows synergistic effects and supports effects and strong electronic interactions at the interfaces, resulting in higher electrocatalytic activities. Zhang et al. synthesized $Co(OH)_2$/NiMo CA@CC as a bifunctional electrocatalyst by the multi-scale optimization of surface/interface engineering induced by large pore arrays that could provide a current density of 10 mA cm^{-2} at a low voltage of 1.52 V [38]. Cheng et al. prepared a NiFe@$Co(OH)_2$ NSAs/NF electrode with a high surface area and high activity through hydrothermal treatment, nickel-iron coating, and the electrodeposition method, achieving an overpotential of 98 mV at 10 mA cm^{-2} and good stability lasting for 20 h [39]. Li et al. constructed the oxide/sulfide heterostructures for N-$NiMoO_4$/NiS_2 nanowires/nanosheets by designing a positive nanoscale heterojunction with well-tuned interfaces that showed excellent overall electrocatalytic water splitting activity with a low voltage of 1.60 V that achieved a current density of 10 mA cm^{-2} [25].

Although $Co(OH)_2$ and α-$NiMoO_4$ have been reported on previously [40–44], their combination to form heterojunction structures and to tune morphologies have not been investigated in depth. Herein, we fabricated a promising hydroxide/oxide heterostructure of $Co(OH)_2$/α-$NiMoO_4$ NWs/CC for the first time through structural design and interface engineering. The α-$NiMoO_4$ nanowires and $Co(OH)_2$ nanoflower structures provide more reaction sites and electron transport channels, enhance the diffusion of electrolytes, and show excellent structural stability, therefore leading to good catalytic activity at large voltages. The $Co(OH)_2$/α-$NiMoO_4$ NWs/CC exhibits excellent HER and OER electrocatalytic activity, with a HER overpotential of 183.01 mV and an OER overpotential of 170.26 mV at 10 mA cm^{-2} in 1.0 KOH. Furthermore, the current of the $Co(OH)_2$/α-$NiMoO_4$ NWs/CC electrode could be maintained for 12 h without an obvious decrease.

2. Results and Discussion

2.1. Surface Morphologies and Structures

The morphologies of α-$NiMoO_4$ NWs/CC and $Co(OH)_2$/α-$NiMoO_4$ NWs/CC were characterized by a scanning electron microscope (SEM). As shown in Figure 1a,b, the α-$NiMoO_4$ NWs exhibit a nanowire structure with a smooth surface and are distributed on the carbon cloth fiber in a network structure with high density, indicating that α-$NiMoO_4$ NWs/CC has been successfully synthesized, which is also consistent with the XRD results. It can be seen from Figure 1c,d that on the surface of $Co(OH)_2$/α-$NiMoO_4$ NWs/CC, there are nanoflowers and nanosheet structures. The nanoflowers grow on the surface of α-$NiMoO_4$ NWs/CC in an orderly manner, and the nanosheets are arranged in a disordered manner on the surface of the nanoflowers. It can be seen that the interwoven carbon fiber, nanowire structure, nanoflower structure, and nanosheet structure have more active sites for chemical reactions and that are conducive to the electrocatalytic reaction and show excellent electrocatalytic performance.

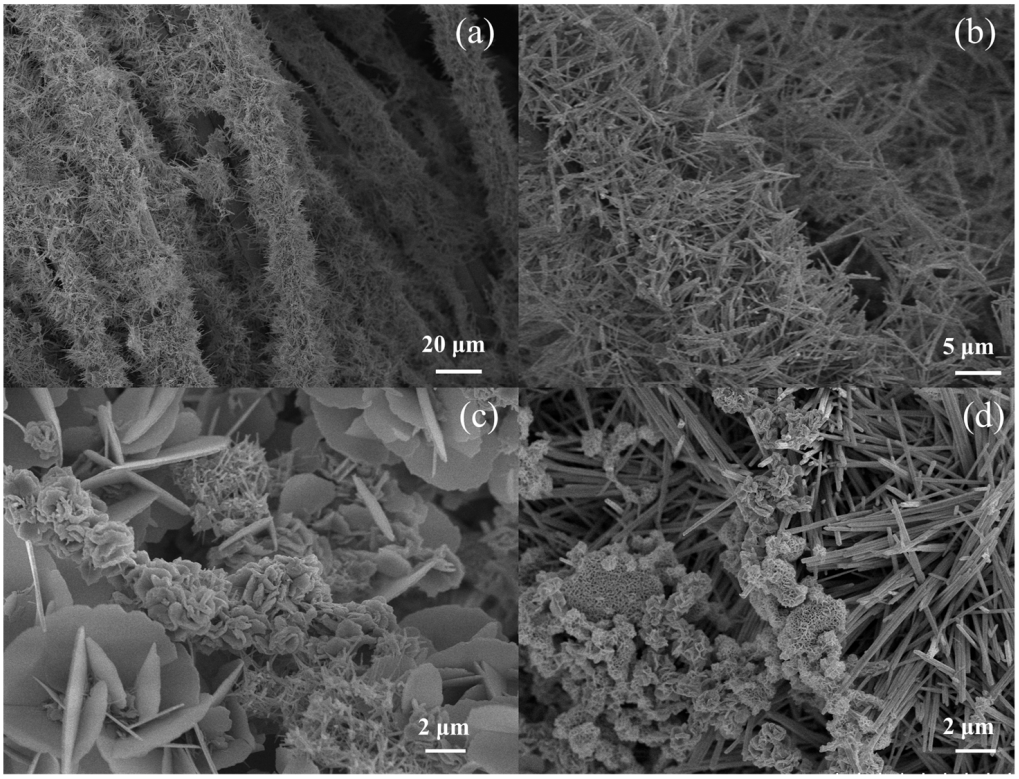

Figure 1. (**a**,**b**) SEM images of α-$NiMoO_4$ NWs/CC; (**c**,**d**) SEM images of $Co(OH)_2$/α-$NiMoO_4$ NWs/CC.

The crystal structures and phases of α-$NiMoO_4$ NWs/CC and $Co(OH)_2$/α-$NiMoO_4$ NWs/CC were characterized by X-ray diffraction (XRD) to analyze the material composition. As shown in Figure 2a, all of the diffraction peaks of the prepared $NiMoO_4$ NWs match well with the Joint Committee on Powder Diffraction Standards (JCPDS) No.86-0361 [25,43], which indicates that the prepared $NiMoO_4$ NWs are α-$NiMoO_4$ NWs with a monoclinic structure. The diffraction peaks of the α-$NiMoO_4$ NWs at 14.34°, 25.40°, 28.91°, 32.66°, 38.84°, 43.97°, 47.51°, 53.45°, 56.80°, 57.85°, and 62.22° correspond to the characteristic peaks of the (110), (112), (220), (−222), (−132), (330), (−204), (150), (024), (−532), and (152) crystal planes, respectively. Moreover, the (111) crystal plane of C corresponding to the diffraction peak at 30.55° is consistent with the standard card JCPDS No. 75-2078 [45], indicating that α-$NiMoO_4$ NWs/CC with a monoclinic structure have been successfully synthesized. In the XRD pattern of the $Co(OH)_2$/α-$NiMoO_4$ NWs/CC, the diffraction peaks at 11.54°, 23.21°, and 34.47° correspond to the characteristic peaks of (003), (006), and (112) on the crystal plane of α-$Co(OH)_2$ (JCPDS No. 46-0605) [46]. The XRD of $Co(OH)_2$/CC was also collected to analyze the material composition in Figure S1. Therefore, the XRD results indicate that the $Co(OH)_2$/α-$NiMoO_4$ NWs/CC synthesized by the hydrothermal method have no diffraction peaks of other phases or impurities compared to the α-$NiMoO_4$ NWs/CC, indicating the successful synthesis of the $Co(OH)_2$/α-$NiMoO_4$ NWs/CC electrocatalyst.

The chemical and bonding states of $Co(OH)_2$/α-$NiMoO_4$ NWs/CC were analyzed by X-ray photoelectron spectroscopy (XPS). In Figure 2b, the XPS survey scan spectrum of the $Co(OH)_2$/α-$NiMoO_4$ NWs/CC confirms the presence of all five elements of Co, Ni, Mo, O, and C. The characteristic peak at 855.70 eV in Figure 2c corresponds to Ni $2p_{3/2}$, the characteristic peak at 873.40 eV corresponds to Ni $2p_{1/2}$, and the energy gap between the two main peaks is 17.7 eV, indicating that Ni mainly exists in the form of Ni^{2+} [47]. Meanwhile, the presence of Ni $2p_{3/2}$ and Ni $2p_{1/2}$ satellite peaks at 861.85 eV and 880.9 eV confirms the existence of electronic association in the system, indicating the interaction between Ni and NiO_6 octahedra in α-$NiMoO_4$ [48]. The characteristic peaks at 232.31 eV

and 235.55 eV in the spectrum of Mo 3d (Figure 2d) correspond to the orbital binding energy of Mo $3d_{5/2}$ and Mo $3d_{3/2}$, respectively, and the position of the two main peaks is that of the characteristic peaks corresponding to the Mo element with a +6 valence [49]. In Figure 2e, the peaks located at 782.58 eV and 797.83 eV could be attributed to $2p_{3/2}$ and $2p_{1/2}$ of the Co element with a +3 valence, and the characteristic peaks at 780.66 eV and 796.38 eV correspond to $2p_{3/2}$ and $2p_{1/2}$ of the Co element with the +2 valence [50]. The highly oxidized Co^{3+} is reported to be the active site of the electrocatalytic OER [51]. In Figure 2f, the characteristic peak at 530.7 eV is attributed to the lattice oxygen metal–O bond in $Co(OH)_2$/α-$NiMoO_4$ NWs/CC. The characteristic peaks at 532.12 eV and 531.30 eV can be attributed to the oxygen species such as water and in the hydroxyl groups adsorbed on the surface of the $Co(OH)_2$/α-$NiMoO_4$ NWs/CC samples. The results are consistent with the XRD and SEM characterization results, further confirming the successful synthesis of the $Co(OH)_2$/α-$NiMoO_4$ NWs/CC electrocatalyst.

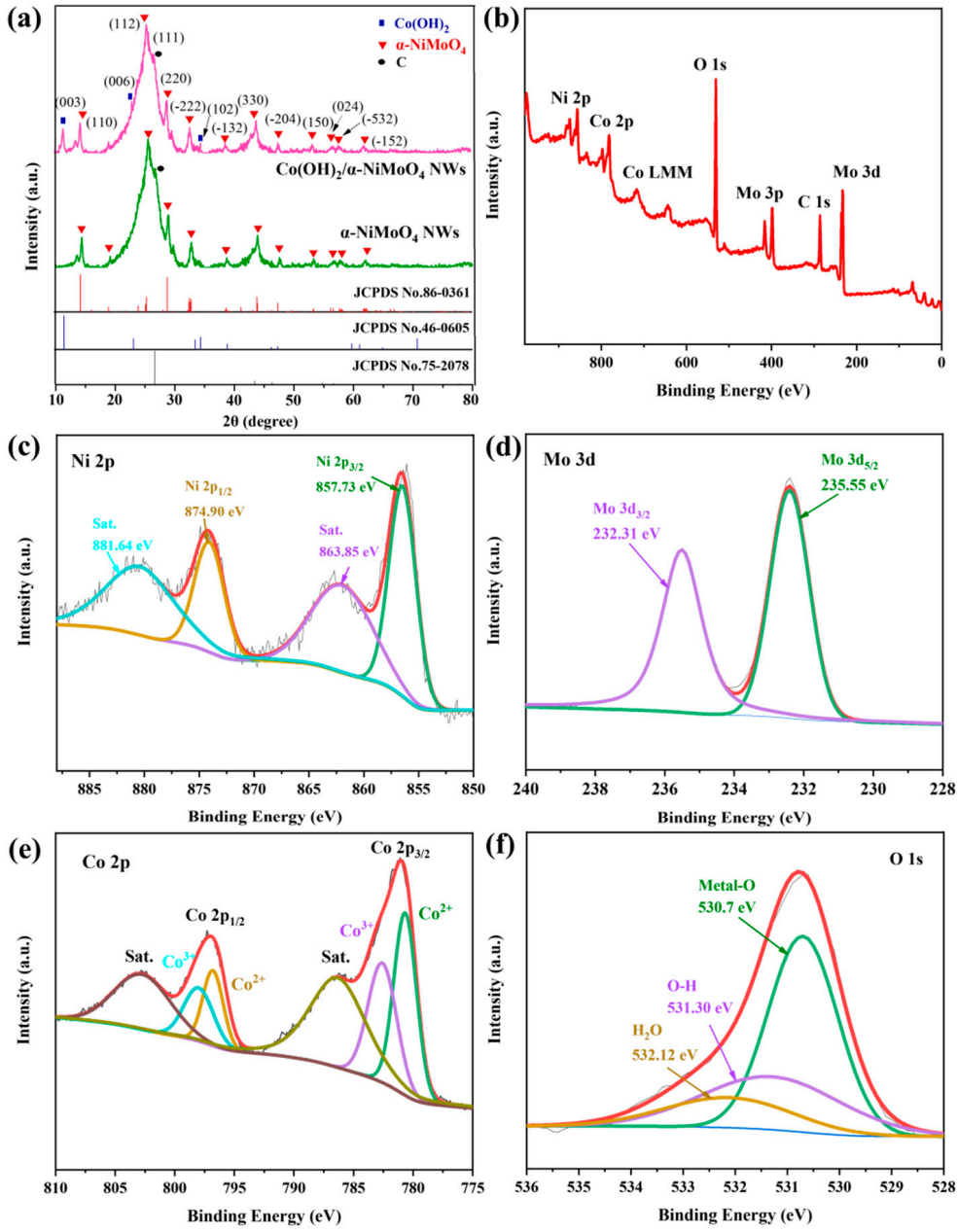

Figure 2. (**a**) XRD patterns of α-$NiMoO_4$ NWs/CC and $Co(OH)_2$/α-$NiMoO_4$ NWs/CC; (**b**) XPS spectra of survey scan; (**c**) Ni 2p; (**d**) Mo 3d; (**e**) Co 2p; (**f**) O 1s of $Co(OH)_2$/α-$NiMoO_4$ NWs/CC.

2.2. Electrocatalytic Performance toward HER

The HER performances were tested in a typical three-electrode system in 1.0 M KOH electrolyte. Before testing, the electrolyte was purged with argon for half an hour to remove the dissolved gas at room temperature. All LSV curves were IR-corrected to eliminate potential loss due to solution resistance. The LSV curves of bare carbon cloth (CC), α-$NiMoO_4$ NWs/CC, and $Co(OH)_2$/α-$NiMoO_4$ NWs/CC were obtained under the same conditions for comparison. As shown in Figure 3a, pure carbon cloth (CC) hardly showed HER performance, while the $Co(OH)_2$/α-$NiMoO_4$ NWs/CC electrode showed the best HER activity. Compared with the 332.93 mV overpotential of α-$NiMoO_4$ NWs/CC, the $Co(OH)_2$/α-$NiMoO_4$ NWs/CC electrode achieved the overpotential of 183.01 mV at 10 mA cm^{-2}. The HER performance of this electrode is better than that of many reported electrocatalysts [52–54]. Moreover, the $Co(OH)_2$/α-$NiMoO_4$ NWs/CC electrode showed better electrocatalytic hydrogen evolution activity as the electric potential increased. Figure 3b listed the required overpotential for the α-$NiMoO_4$ NWs/CC and $Co(OH)_2$/α-$NiMoO_4$ NWs/CC electrocatalysts at different current densities. The $Co(OH)_2$/CC was also used as an electrode for electrochemical water splitting, for which a comparison can be seen in Figure S2. It can be concluded that the $Co(OH)_2$/α-$NiMoO_4$ NWs/CC electrode requires the lowest overpotential and has the best electrocatalytic hydrogen evolution performance at the same current density. This is mainly because the simultaneous introduction of Mo and Ni elements will move down the d band of Mo to the Fermi level, which causes the hydrogen adsorption energy to be in a favorable state and promotes the formation of hydrogen molecules.

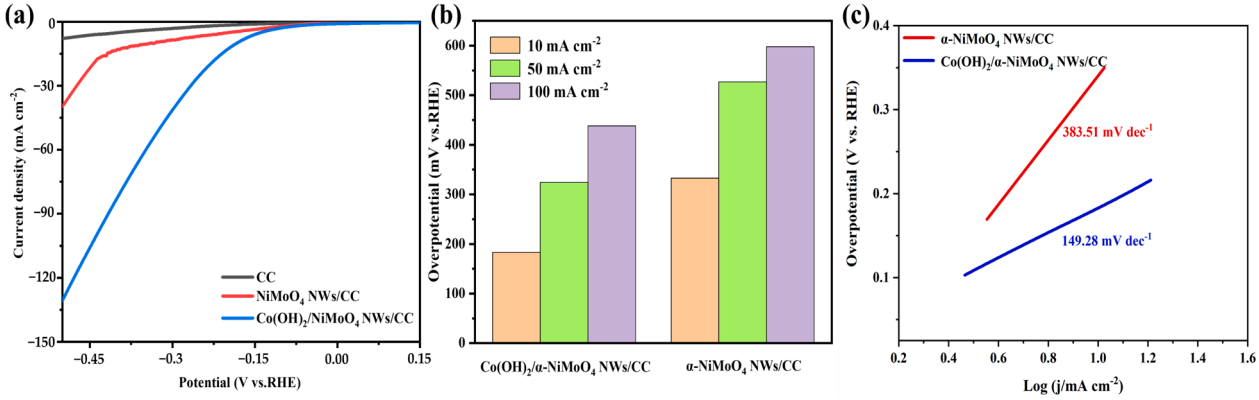

Figure 3. (**a**) LSV curves of different catalysts; (**b**) the overpotential for α-$NiMoO_4$ NWs/CC and $Co(OH)_2$/α-$NiMoO_4$ NWs/CC to reach different current densities in a catalytic reaction; (**c**) Tafel curves of α-$NiMoO_4$ NWs/CC and $Co(OH)_2$/α-$NiMoO_4$ NWs/CC.

The Tafel slope curves were obtained by fitting the LSV curves with the Tafel equation. The kinetic mechanism for the electrocatalytic hydrogen evolution of the $Co(OH)_2$/α-$NiMoO_4$ NWs/CC electrode was studied. As shown in Figure 3c, the Tafel slope of the $Co(OH)_2$/α-$NiMoO_4$ NWs/CC electrocatalyst is 149.28 mV dec^{-1}, which is significantly smaller than that of α-$NiMoO_4$ NWs/CC (383.51 mV dec^{-1}). These results indicate that the $Co(OH)_2$/α-$NiMoO_4$ NWs/CC electrode exhibits faster electrocatalytic kinetics of hydrogen evolution. The exchange current density j_0 was extrapolated from the Tafel slope curve. The exchange current density j_0 of the $Co(OH)_2$/α-$NiMoO_4$ NWs/CC electrocatalyst was 0.31 mA cm^{-2}, which was much larger than that of α-$NiMoO_4$ NWs/CC (0.16 mA cm^{-2}). The results show that the $Co(OH)_2$/α-$NiMoO_4$ NWs/CC electrode has faster HER kinetic parameters.

The double layer capacitance (C_{dl}) of the -$NiMoO_4$ NWs/CC and $Co(OH)_2$/-$NiMoO_4$ NWs/CC electrodes were tested in a non-Faraday region in order to further explore the cause of the high electrocatalytic activity of the as-prepared electrode samples. The C_{dl} were calculated by recording a series of cyclic voltammograms of the α-$NiMoO_4$

NWs/CC and $Co(OH)_2$/α-$NiMoO_4$ NWs/CC electrocatalysts at different scanning rates of 10~120 mV s^{-1} in the scanning range of 0.12~0.24 V vs. RHE. As shown in Figure 4c, the C_{dl} of the $Co(OH)_2$/α-$NiMoO_4$ NWs/CC electrode is 35.49 mF cm^{-2}, which is about 2.35 times that of α-$NiMoO_4$ NWs/CC (C_{dl} is 15.08 mF cm^{-2}). The results show that the $Co(OH)_2$/α-$NiMoO_4$ NWs/CC electrocatalyst has better electrocatalytic hydrogen evolution performance due to its unique structures of nanowires and nanoflowers, which increase the specific surface area and active sites. In addition, the semicircular region of the EIS curve represents the charge transport resistance of the electrocatalyst, and the linear region represents the diffusion resistance. Figure 4d shows the electrochemical impedance spectra of the α-$NiMoO_4$ NWs/CC and $Co(OH)_2$/α-$NiMoO_4$ NWs/CC electrocatalysts. The smaller arc radius of the $Co(OH)_2$/α-$NiMoO_4$ NWs/CC electrocatalyst indicates the lower charge transfer resistance. Hence, the introduction of $Co(OH)_2$ nanoflowers on α-$NiMoO_4$ NWs/CC is beneficial to the charge transfer resistance, which is conducive to the electrocatalytic hydrogen evolution reaction.

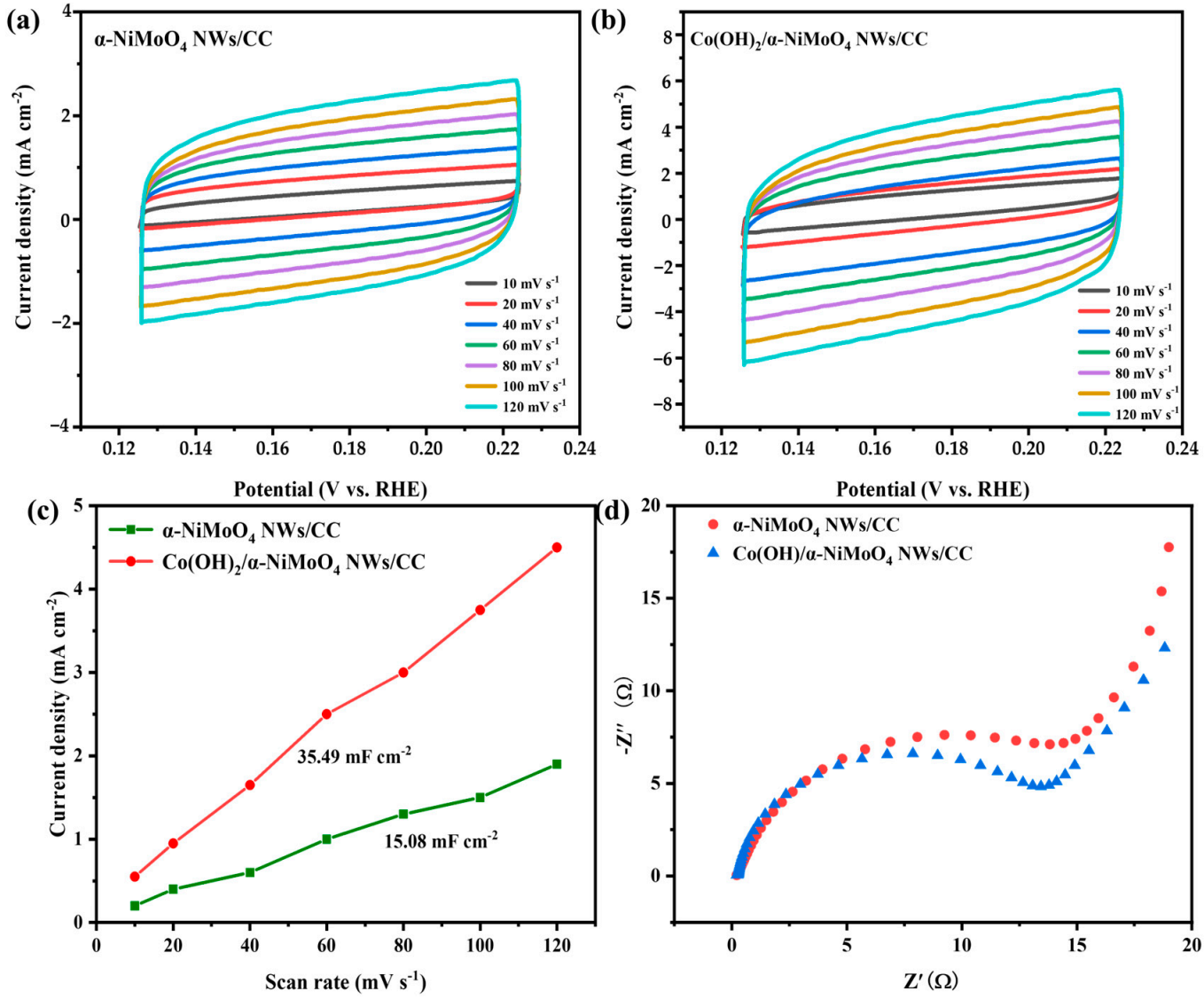

Figure 4. (**a**) CV of α-$NiMoO_4$ NWs/CC catalyst at different sweep rates; (**b**) CV of $Co(OH)_2$/α-$NiMoO_4$ NWs/CC catalyst at different sweep rates; (**c**) function of capacitance current and scanning rate and (**d**) EIS of α-$NiMoO_4$ NWs/CC and $Co(OH)_2$/α-$NiMoO_4$ NWs/CC.

The electrocatalytic activity and stability of the $Co(OH)_2$/α-$NiMoO_4$ NWs/CC electrode were investigated as well. As shown in Figure 5a, the polarization curve of the

$Co(OH)_2/\alpha$-$NiMoO_4$ NWs/CC electrode after 1000 CV cycles almost coincides with the initial polarization curve, confirming the stable electrocatalytic hydrogen evolution performance of the $Co(OH)_2/\alpha$-$NiMoO_4$ NWs/CC electrode. Similarly, the current density produced by the $Co(OH)_2/\alpha$-$NiMoO_4$ NWs/CC electrode at −0.40 V vs. RHE for 6 h is almost unchanged without obvious potential loss, as shown in Figure 5b, which also indicates the good electrochemical stability of the $Co(OH)_2/\alpha$-$NiMoO_4$ NWs/CC electrode.

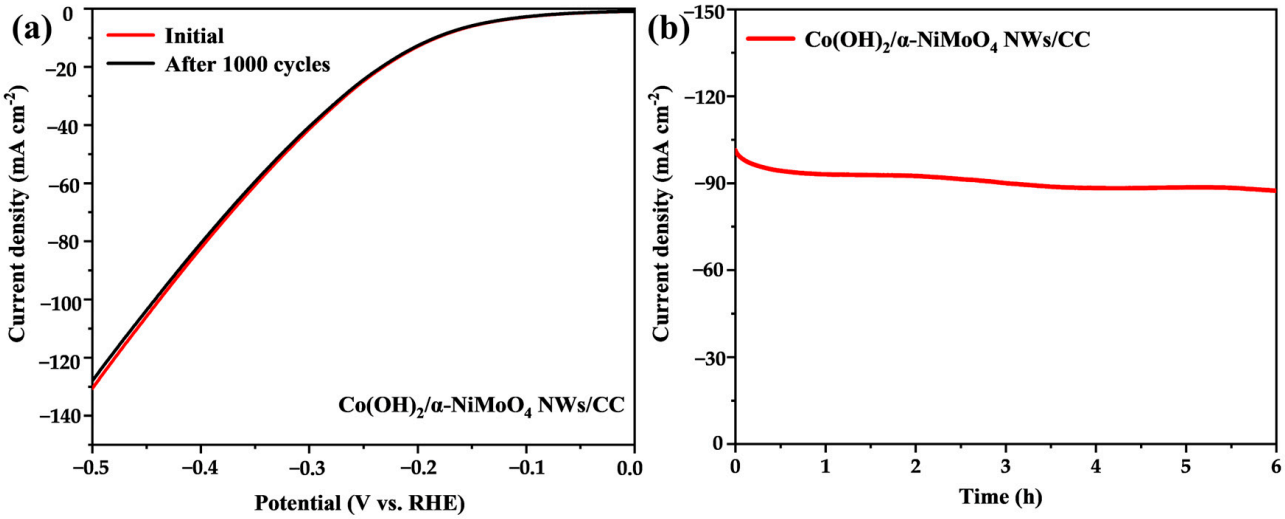

Figure 5. (**a**) LSV curves of $Co(OH)_2/\alpha$-$NiMoO_4$ NWs/CC electrocatalysts after 1000 cycles of CV; (**b**) stability of $Co(OH)_2/\alpha$-$NiMoO_4$ NWs/CC electrocatalysts at −0.40 V vs. RHE.

2.3. Electrocatalytic Performance toward OER

Electrocatalytic oxygen evolution (OER) is regarded as the bottleneck of electrocatalytic water splitting due to the characteristics of slow kinetics and a variety of intermediates. The OER performances of pure carbon cloth, α-$NiMoO_4$ NWs/CC, and $Co(OH)_2/\alpha$-$NiMoO_4$ NWs/CC were tested in alkaline conditions. According to the LSV curves in Figure 6a, bare carbon cloth still has no OER activity at higher current densities. The $Co(OH)_2/\alpha$-$NiMoO_4$ NWs/CC electrode shows the lowest overpotential of 170.26 mV at the current density of 10 mA cm^{-2}, which is 109.87 mV less than α-$NiMoO_4$ NWs/CC. As indicated in the XPS spectra, the Ni in α-$NiMoO_4$ mainly exists in the form of Ni^{2+} and shows interaction between Ni and NiO_6 octahedra. The oxidation peak at around 1.5 V in the OER data (LSV) of α-$NiMoO_4$ NWs/CC can be attributed to the electrochemical oxidation of Ni^{+2} to Ni^{+3}. For $Co(OH)_2/\alpha$-$NiMoO_4$ NWs/CC, the oxidation peak at around 1.5 V is also related to the electrochemical oxidation of Ni^{+2} to Ni^{+3}, while the oxidation peak at a lower potential (∼1.26 V) can be assigned to the oxidation of Co^{+2} to Co^{+3}. As shown in Figure 6b, the $Co(OH)_2/\alpha$-$NiMoO_4$ NWs/CC electrocatalyst requires the lowest overpotential at the same current density and has the best performance regarding electrocatalytic oxygen evolution. According to the XRD and XPS analyses, the $Co(OH)_2$ introduced in α-$NiMoO_4$ NWs/CC contains Co^{3+}. The active site for electrocatalytic OER is the high-valence Co atom, which has a favorable role in boosting electrocatalytic OER [51]. Furthermore, when compared to the LSV polarization curves, the $Co(OH)_2/\alpha$-$NiMoO_4$ NWs/CC electrode exhibits an apparent oxidation peak at 1.5 V vs. RHE, implying that Co^{2+} is constantly oxidized to Co^{3+} via a continuous reaction. In Figure 6c, the $Co(OH)_2/\alpha$-$NiMoO_4$ NWs/CC has a substantially lower Tafel slope of 148.95 mV dec^{-1} than α-$NiMoO_4$ NWs/CC (220.11 mV dec^{-1}), indicating the fastest OER kinetics. The $Co(OH)_2$/CC was also used as an electrode in electrochemical water splitting, and a comparison can be seen in Figure S3.

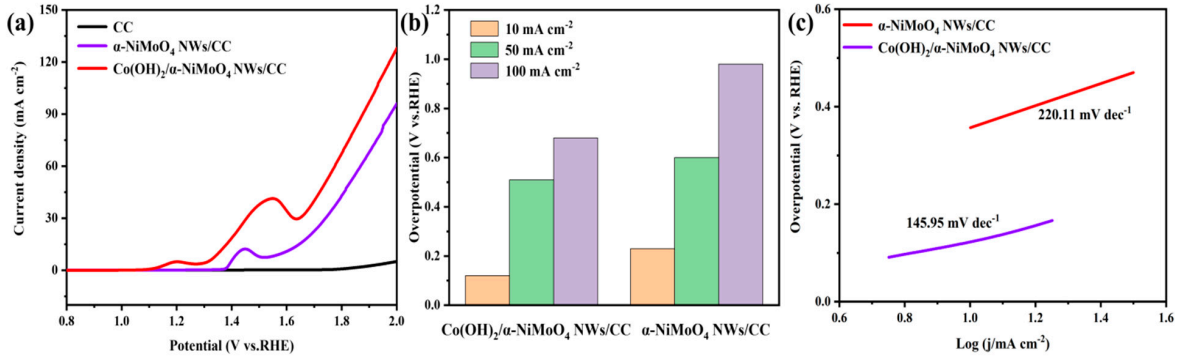

Figure 6. (**a**) LSV curves of different catalysts for OER; (**b**) the overpotential for α-$NiMoO_4$ NWs/CC and $Co(OH)_2$/α-$NiMoO_4$ NWs/CC to reach different current densities of OER; (**c**) Tafel curves of α-$NiMoO_4$ NWs/CC and $Co(OH)_2$/α-$NiMoO_4$ NWs/CC.

The C_{dl} of the $Co(OH)_2$/α-$NiMoO_4$ NWs/CC electrode was studied in the non-Faraday region to further investigate the reason for the high electrocatalytic activity of the $Co(OH)_2$/α-$NiMoO_4$ NWs/CC electrocatalyst. The C_{dl} was estimated by recording a series of cyclic voltammograms of the α-$NiMoO_4$ NWs/CC (Figure 7a) and $Co(OH)_2$/α-$NiMoO_4$ NWs/CC (Figure 7b) electrocatalysts at varied scanning rates of 10~120 mV s^{-1} in the scanning range of 0.82~0.94 V vs. RHE. As shown in Figure 7c, the C_{dl} of the $Co(OH)_2$/α-$NiMoO_4$ NWs/CC electrocatalyst is 41.09 mF cm^{-2}, which is approximately 1.67 times that of α-$NiMoO_4$ NWs/CC (C_{dl} is 24.6 mF cm^{-2}). The results indicate that the $Co(OH)_2$/α-$NiMoO_4$ NWs/CC electrocatalyst performs better regarding electrocatalytic oxygen evolution. As shown in Figure 7d, the lowest R_{ct} value of $Co(OH)_2$/α-$NiMoO_4$ NWs/CC implies lower charge transfer resistance and faster electron transport, which improves OER kinetics.

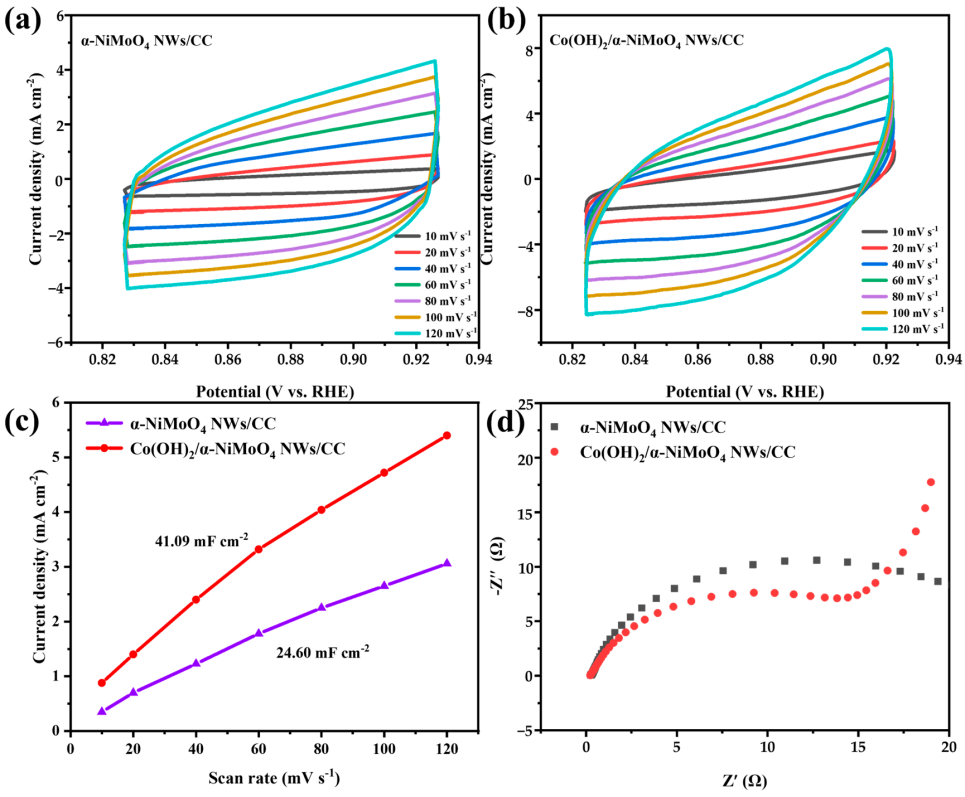

Figure 7. (**a**,**b**) CV of α-$NiMoO_4$ NWs/CC and $Co(OH)_2$/α-$NiMoO_4$ NWs/CC catalyst at varied scan rate and potential range; (**c**) function of capacitance current and scanning rate and (**d**) EIS of α-$NiMoO_4$ NWs/CC and $Co(OH)_2$/α-$NiMoO_4$ NWs/CC.

After 1000 cycles of the CV cycle, the polarization curve of the $Co(OH)_2/\alpha$-$NiMoO_4$ NWs/CC electrode approximately coincides with the original polarization curve, as shown in Figure 8a, indicating that the electrocatalytic oxygen evolution performance of the $Co(OH)_2/\alpha$-$NiMoO_4$ NWs/CC electrocatalyst is almost not weakened. Additionally, compared to the original material, the $Co(OH)_2/\alpha$-$NiMoO_4$ NWs/CC electrocatalyst shows improved OER performance, demonstrating that Co^{2+} is constantly oxidized to Co^{3+} via the continuous reaction, which is also consistent with the prior test. The current density generated by the $Co(OH)_2/\alpha$-$NiMoO_4$ NWs/CC electrocatalyst at +1.23 V vs. RHE for 12 h is nearly unchanged, as shown in Figure 8b.

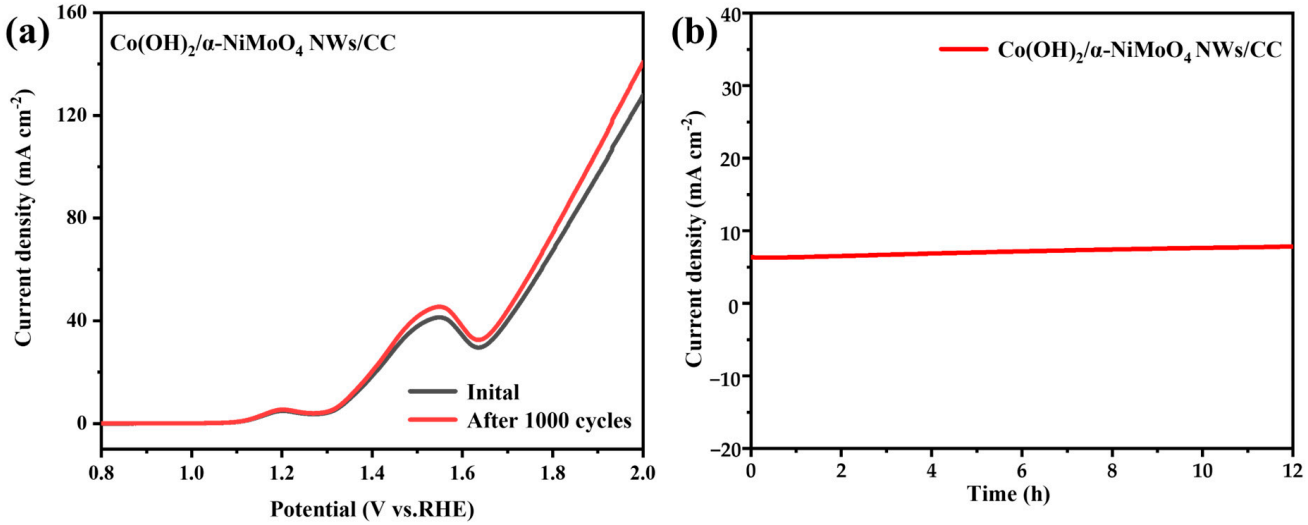

Figure 8. (**a**) Polarization curves LSV of $Co(OH)_2/\alpha$-$NiMoO_4$ NWs/CC electrocatalysts after 1000 cycles of CV; (**b**) stability of $Co(OH)_2/\alpha$-$NiMoO_4$ NWs/CC electrocatalysts at +1.23 V vs. RHE.

As the OER and HER results indicate the good performance of $Co(OH)_2/\alpha$-$NiMoO_4$ NWs/CC, we further compared them with various other Co-, Ni-, and Mo-based electrocatalysts in 1 M KOH at the current density of 10 mA/cm^2. As shown in Table 1, the as-prepared $Co(OH)_2/\alpha$-$NiMoO_4$ NWs/CC electrode shows better OER performance than most other Co-, Ni-, and Mo-based electrocatalysts.

Table 1. Comparison of the OER and HER performances of $Co(OH)_2/\alpha$-$NiMoO_4$ NWs/CC with other Co-, Ni-, Mo-based electrocatalysts in 1 M KOH at a current density of 10 mA/cm^2.

Composites.	OER Overpotential (mV vs. RHE)	HER Overpotential (mV vs. RHE)	References
$Co(OH)_2/\alpha$-$NiMoO_4$ NWs/CC	170	183	This work
Mo-$Co(OH)_2$ HNTs	218	125	[50]
$NiMoO_4$/NF	310	95	[55]
Ni_9S_8/MoS_2	360	190	[56]
a-$Co(OH)_2$	270	260	[57]
$NiMoO_4$ $1/2H_2O$-NRs	360	166	[58]
$Cu_2SeCo(OH)_2$	268	241	[33]

3. Experimental

3.1. Materials

The nitric acid (HNO_3), nickel sulfate hexahydrate ($NiSO_4 \cdot 6H_2O$), sodium molybdate dihydrate ($Na_2MoO_4 \cdot 2H_2O$), potassium permanganate ($KMnO_4$, 5%), hexamethylenetetramine (HMT), ethanol (AR, >99.7%), and acetone (AR, >99.5%) were purchased from

Sinopharm Chemical Reagent Co., Ltd., Shanghai, China. The cobalt chloride hexahydrate ($CoCl_2 \cdot 6H_2O$) was purchased from Shanghai Macklin Biochemical Co., Ltd., Shanghai, China. Deionized water (DI) was used in the experiments.

3.2. Synthesis of α-$NiMoO_4$ NWs/CC

Before preparation, the carbon cloth was cut into 1 cm × 2 cm pieces, cleaned by ultrasound in 0.25 mol L^{-1} HNO_3 solution, absolute ethanol, and deionized water for 30 min, and then dried at 60 °C. The α-$NiMoO_4$ NWs/CC was synthesized via a hydrothermal process and calcination method. Briefly, a precursor solution was obtained by dissolving 2.5 mmol of $NiSO_4 \cdot 6H_2O$ and 2.5 mmol of $Na_2MoO_4 \cdot 2H_2O$ in 50 mL of deionized water with magnetic stirring for 45 min. The precursor solution was then transferred into a 100 mL polytetrafluoro-ethylene autoclave. The cleaned carbon cloth substrate was soaked in 5% $KMnO_4$ solution for 30 min and was hung in the Teflon-lined autoclave using a PTFE sewing thread. The autoclave was kept at a constant temperature of 150 °C for 6 h in an oven and then cooled to room temperature naturally. Subsequently, the sample was soaked in acetone for 5 min to remove residual nanoparticle debris, washed several times with ethanol and deionized water, and then dried at 60 °C in a vacuum oven. Finally, the dried samples were put into the tube furnace and were heated from room temperature to 400 °C under an argon atmosphere with a heating rate of 2 °C min^{-1}. After annealing for 2 h, light green $NiMoO_4$ nanowires on the carbon cloth (denoted as α-$NiMoO_4$ NWs/CC) were obtained.

3.3. Synthesis of $Co(OH)_2$/α-$NiMoO_4$ NWs/CC

In the next step, 0.5 mmol of HMT and 1 mmol of $CoCl_2 \cdot 6H_2O$ were added into 40 mL of deionized water and underwent magnetic stirring for 30 min, obtaining a precursor solution. Then, the above-prepared solution was transferred to the Teflon-lined autoclave and the as-prepared α-$NiMoO_4$ NWs/CC was being hung by a PTFE sewing thread. After hydrothermal treatment at 90 °C for 150 min, a green $Co(OH)_2$/α-$NiMoO_4$ NWs/CC was obtained and washed with deionized water and then vacuum-dried at 60 °C for 24 h. The $Co(OH)_2$/CC was also obtained in the same procedure. The preparation process of the electrocatalyst was as illustrated in Scheme 1.

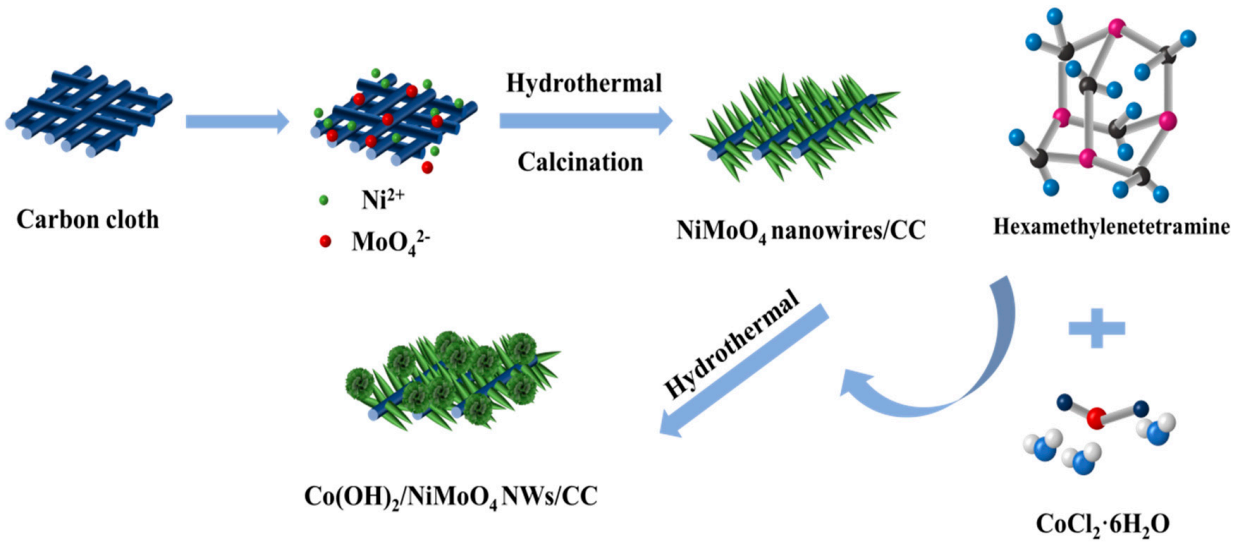

Scheme 1. The synthesis procedure of $Co(OH)_2$/α-$NiMoO_4$ NWs/CC samples.

3.4. Characterization

Crystal structures and phases were characterized by X-ray diffraction (XRD, Bruker AXS-D8, Ettlingen, Germany) with Cu Kα radiation. Microscopic morphologies were observed by a scanning electron microscope (SEM, Hitachi S-4800, Tokyo, Japan). The

chemical state of each element in the samples was characterized by an X-ray photoelectron spectroscope (XPS, Thermo Scientific K-Alpha$^+$, Waltham, MA, USA) using C 1s signals at the binding energy of 284.6 eV as a reference.

3.5. Electrochemical Measurements

Both the HER and OER electrochemical tests were accomplished on an electrochemical workstation (CHI660E, Shanghai CH Instruments Co., Shanghai, China) using a three-electrode system with the as-prepared electrodes as the working electrode, a Pt electrode a as counter electrode, and a saturated Ag/AgCl electrode as a reference electrode in 1 M KOH electrolyte. Linear sweep voltammetry (LSV) curves were measured with a scan rate of 5 mV s^{-1}, with the relatively slow scanning rate being able to reduce the faraday current. For the electrocatalytic hydrogen evolution reaction (HER), linear sweep voltammetric (LSV) tests were conducted in a specific bias range of −2~1 V, while for the electrocatalytic oxygen evolution reaction (OER), the voltage sweep range was −1~0.8 V. The Tafel slope could be obtained from the LSV curve of the experimental data according to the Tafel equation $\eta = a + b \log j$ (where η is the overpotential, a is the charge transfer coefficient, b is the Tafel slope, and j is the current density). A lower Tafel slope and higher exchange current density j_0 can reflect the difficulty of electron transfer at the interface. To measure the electrochemical capacitance of the catalysts, cyclic voltammetry (CV) tests were conducted with different scan rates ranging from 10 to 100 mV s^{-1}. The potential was in the range of 0.82~0.84 V vs. RHE for HER and in the range of 0.12~0.24 V vs. RHE for OER. Electrochemical impedance spectroscopy (EIS) was obtained with frequencies ranging from 0.01 Hz to 10^5 Hz and with an amplitude of 10 mV at an open-circuit potential. The electrochemical stability of the catalysts was tested by recording the changes in the LSV curve before and after the catalysts were continuously cycled 1000 times by CV, and the current density–time curves of the catalysts at −0.4 V vs. RHE (for HER) and 1.23 V vs. RHE (for OER) were tested by chronoamperometry (CA). All of the measured potentials were converted to the reversible hydrogen electrode (RHE) scale by the Nernst equation: $E_{RHE} = E_{Ag/AgCl} + 0.197 + 0.059$ pH [59–61]. The overpotential of the hydrogen evolution reaction was equal to the reversible hydrogen electrode. The overpotential of the oxygen evolution reaction was converted by the formula $\eta = E_{RHE} - 1.23$. The Tafel equation is $\eta = a + b \log j$, where η is the overpotential, a is the charge transfer coefficient, b is the Tafel slope, and j is the current density.

4. Conclusions

In conclusion, we fabricated novel hydroxide/oxide heterostructures of $Co(OH)_2$/α-$NiMoO_4$ NWs on carbon cloth substrates for electrocatalytic water splitting. The $Co(OH)_2$/α-$NiMoO_4$ NWs/CC electrode showed excellent electrocatalytic HER and OER activity and good stability, with overpotentials of 183.01 mV for HER and 170.26 mV for OER at a current density of 10 mA cm^{-2}. The enhanced performances could be attributed to the following aspects: (1) The $NiMoO_4$ nanowire array and the decorated $Co(OH)_2$ nanoflowers provide open space for diffusion as well as a large surface area and active sites for electrocatalytic reactions. (2) The +3 valent Co element exhibits a tendency to considerably improve the performance of OER. This work provides some references for the preparation of cobalt–molybdenum-based bifunctional catalysts for electrocatalytic water splitting.

Supplementary Materials: The following supporting information can be downloaded at: https://www.mdpi.com/article/10.3390/catal12111417/s1, Figure S1: XRD pattern of $Co(OH)_2$/CC, Figure S2: LSV curves of different catalysts for HER, Figure S3: LSV curves of different catalysts for OER.

Author Contributions: Conceptualization, W.W., C.L. and Z.X.; methodology, M.H. and Z.X.; validation, M.H., Z.X. and L.W.; formal analysis, X.L. and Z.X.; investigation, Z.X.; resources, L.W. and C.L.; data curation, Z.X.; writing—original draft preparation, Z.X.; writing—review and editing, W.W.;

visualization, Z.X.; supervision, W.W. and C.L.; project administration, J.M.; funding acquisition, W.W. All authors have read and agreed to the published version of the manuscript.

Funding: This research was funded by Natural Science Foundation of Shandong Province (grant number ZR2021MB075); the Opening Fund of State Key Laboratory of High-efficiency Utilization of Coal and Green Chemical Engineering (grant number 2021-K53).

Acknowledgments: Partial financial support was received for this collaborative work from the Natural Science Foundation of Shandong Province (ZR2021MB075) and from the Opening Fund of State Key Laboratory of High-efficiency Utilization of Coal and Green Chemical Engineering (2021-K53).

Conflicts of Interest: The authors declare no conflict of interest.

References

1. Li, X.; Zhao, L.; Yu, J.; Liu, X.; Zhang, X.; Liu, H.; Zhou, W. Water Splitting: From Electrode to Green Energy System. *Nanomicro Lett.* **2020**, *12*, 131. [CrossRef] [PubMed]
2. Liu, X.; Chi, J.; Dong, B.; Sun, Y. Recent Progress in Decoupled H_2 and O_2 Production from Electrolytic Water Splitting. *ChemElectroChem* **2019**, *6*, 2157–2166. [CrossRef]
3. Guo, Z.; Liu, L.; Wang, J.; Cao, Y.; Tu, J.; Zhang, X.; Ding, L. Recent progress in CoP-based materials for electrochemical water splitting. *Int. J. Hydrogen Energy* **2021**, *46*, 34194–34215. [CrossRef]
4. Zhou, D.; Li, P.; Xu, W.; Jawaid, S.; Mohammed-Ibrahim, J.; Liu, W.; Kuang, Y.; Sun, X. Recent Advances in Non–Precious Metal–Based Electrodes for Alkaline Water Electrolysis. *ChemNanoMat* **2020**, *6*, 336–355. [CrossRef]
5. You, B.; Tang, M.T.; Tsai, C.; Abild-Pedersen, F.; Zheng, X.; Li, H. Enhancing Electrocatalytic Water Splitting by Strain Engineering. *Adv. Mater.* **2019**, *31*, 1807001. [CrossRef] [PubMed]
6. Yan, Y.; Xia, B.Y.; Zhao, B.; Wang, X. A review on noble-metal-free bifunctional heterogeneous catalysts for overall electrochemical water splitting. *J. Mater. Chem. A* **2016**, *4*, 17587–17603. [CrossRef]
7. Zhao, G.; Rui, K.; Dou, S.X.; Sun, W. Heterostructures for Electrochemical Hydrogen Evolution Reaction: A Review. *Adv. Funct. Mater.* **2018**, *28*, 1803291. [CrossRef]
8. Lv, X.; Wei, W.; Wang, H.; Huang, B.; Dai, Y. Multifunctional electrocatalyst PtM with low Pt loading and high activity towards hydrogen and oxygen electrode reactions: A computational study. *Appl. Catal. B-Environ.* **2019**, *255*, 117743. [CrossRef]
9. Lai, W.; Zhang, L.; Hua, W.; Indris, S.; Yan, Z.; Hu, Z.; Zhang, B.; Liu, Y.; Wang, L.; Liu, M.; et al. General pi-Electron-Assisted Strategy for Ir, Pt, Ru, Pd, Fe, Ni Single-Atom Electrocatalysts with Bifunctional Active Sites for Highly Efficient Water Splitting. *Angew. Chem.-Int. Ed.* **2019**, *58*, 11868–11873. [CrossRef]
10. You, B.; Sun, Y. Innovative Strategies for Electrocatalytic Water Splitting. *Acc. Chem. Res.* **2018**, *51*, 1571–1580. [CrossRef]
11. Zhang, L.; Jang, H.; Liu, H.; Kim, M.G.; Yang, D.; Liu, S.; Liu, X.; Cho, J. Sodium-Decorated Amorphous/Crystalline RuO_2 with Rich Oxygen Vacancies: A Robust pH-Universal Oxygen Evolution Electrocatalyst. *Angew. Chem.-Int. Ed.* **2021**, *60*, 18821–18829. [CrossRef] [PubMed]
12. Sun, H.; Yan, Z.; Liu, F.; Xu, W.; Cheng, F.; Chen, J. Self-Supported Transition-Metal-Based Electrocatalysts for Hydrogen and Oxygen Evolution. *Adv. Mater.* **2020**, *32*, 1806326. [CrossRef] [PubMed]
13. Joo, J.; Kim, T.; Lee, J.; Choi, S.-I.; Lee, K. Morphology-Controlled Metal Sulfides and Phosphides for Electrochemical Water Splitting. *Adv. Mater.* **2019**, *31*, 1806682. [CrossRef] [PubMed]
14. Dionigi, F.; Zhu, J.; Zeng, Z.; Merzdorf, T.; Sarodnik, H.; Gliech, M.; Pan, L.; Li, W.; Greeley, J.; Strasser, P. Intrinsic Electrocatalytic Activity for Oxygen Evolution of Crystalline 3d-Transition Metal Layered Double Hydroxides. *Angew. Chem. Int. Ed. Engl.* **2021**, *60*, 14446–14457. [CrossRef] [PubMed]
15. Guo, Y.; Park, T.; Yi, J.W.; Henzie, J.; Kim, J.; Wang, Z.; Jiang, B.; Bando, Y.; Sugahara, Y.; Tang, J.; et al. Nanoarchitectonics for Transition-Metal-Sulfide-Based Electrocatalysts for Water Splitting. *Adv. Mater.* **2019**, *31*, 1807134. [CrossRef]
16. Pang, J.; Mendes, R.G.; Bachmatiuk, A.; Zhao, L.; Ta, H.Q.; Gemming, T.; Liu, H.; Liu, Z.; Rummeli, M.H. Applications of 2D MXenes in energy conversion and storage systems. *Chem. Soc. Rev.* **2019**, *48*, 72–133. [CrossRef]
17. Han, Q.; Fan, L.; Wan, H. Recent Development of Metal Alloy Nanostructures for Electrochemical Hydrogen Generation. *Int. J. Electrochem. Sci.* **2019**, *14*, 11549–11559. [CrossRef]
18. Lu, F.; Zhou, M.; Zhou, Y.; Zeng, X. First-Row Transition Metal Based Catalysts for the Oxygen Evolution Reaction under Alkaline Conditions: Basic Principles and Recent Advances. *Small* **2017**, *13*, 1701931. [CrossRef]
19. Wang, J.; Yue, X.; Yang, Y.; Sirisomboonchai, S.; Wang, P.; Ma, X.; Abudula, A.; Guan, G. Earth-abundant transition-metal-based bifunctional catalysts for overall electrochemical water splitting: A review. *J. Alloys Compd.* **2020**, *819*, 153346. [CrossRef]
20. Li, Y.; Dong, Z.; Jiao, L. Multifunctional Transition Metal-Based Phosphides in Energy-Related Electrocatalysis. *Adv. Energy Mater.* **2020**, *10*, 1902104. [CrossRef]
21. Chen, S.; Qiao, S.-Z. Hierarchically Porous Nitrogen-Doped Graphene-$NiCo_2O_4$ Hybrid Paper as an Advanced Electrocatalytic Water-Splitting Material. *ACS Nano* **2013**, *7*, 10190–10196. [CrossRef] [PubMed]

22. Xiao, C.; Li, Y.; Lu, X.; Zhao, C. Bifunctional Porous NiFe/$NiCo_2O_4$/Ni Foam Electrodes with Triple Hierarchy and Double Synergies for Efficient Whole Cell Water Splitting. *Adv. Funct. Mater.* **2016**, *26*, 3515–3523. [CrossRef]
23. Gong, Y.; Yang, Z.; Lin, Y.; Wang, J.; Pan, H.; Xu, Z. Hierarchical heterostructure $NiCo_2O_4$@$CoMoO_4$/NF as an efficient bifunctional electrocatalyst for overall water splitting. *J. Mater. Chem. A* **2018**, *6*, 16950–16958. [CrossRef]
24. Wang, J.; Hu, J.; Liang, C.; Chang, L.; Du, Y.; Han, X.; Sun, J.; Xu, P. Surface reconstruction of phosphorus-doped cobalt molybdate microarrays in electrochemical water splitting. *Chem. Eng. J.* **2022**, *446*, 137094. [CrossRef]
25. An, L.; Feng, J.; Zhang, Y.; Wang, R.; Liu, H.; Wang, G.; Cheng, F.; Xi, P. Epitaxial Heterogeneous Interfaces on N-$NiMoO_4$/NiS_2 Nanowires/Nanosheets to Boost Hydrogen and Oxygen Production for Overall Water Splitting. *Adv. Funct. Mater.* **2019**, *29*, 1805298. [CrossRef]
26. Choi, J.; Kim, D.; Zheng, W.; Yan, B.; Li, Y.; Lee, L.Y.S.; Piao, Y. Interface engineered $NiFe_2O_{4-x}$/$NiMoO_4$ nanowire arrays for electrochemical oxygen evolution. *Appl. Catal. B-Environ.* **2021**, *286*, 119857. [CrossRef]
27. Kim, T.-G.; Samuel, E.; Park, C.-W.; Joshi, B.; Kim, M.-W.; Swihart, M.; Yoon, S. Supersonically sprayed Zn_2SnO_4/SnO_2/carbon nanotube films for high-efficiency water splitting photoanodes. *J. Alloys Compd.* **2020**, *828*, 154374. [CrossRef]
28. Zhou, M.; Zeng, Y.; Liu, Y.; Sun, Y.; Lu, F.; Zhang, X.; Cao, R.; Xue, Y.; Zeng, X.; Wu, Y. Ni-Mo based metal/oxide heterostructured nanosheets with largely exposed interfacial atoms for overall water-splitting. *Appl. Surf. Sci.* **2022**, *597*, 153597. [CrossRef]
29. Liu, Q.; Wang, E.; Sun, G. Layered transition-metal hydroxides for alkaline hydrogen evolution reaction. *Chin. J. Catal.* **2020**, *41*, 574–591. [CrossRef]
30. Yoon, T.; Kim, K.S. One-Step Synthesis of CoS-Doped beta-$Co(OH)_2$@Amorphous MoS_{2+x} Hybrid Catalyst Grown on Nickel Foam for High-Performance Electrochemical Overall Water Splitting. *Adv. Funct. Mater.* **2016**, *26*, 7386–7393. [CrossRef]
31. Sapountzi, F.M.; Gracia, J.M.; Weststrate, C.J.; Fredriksson, H.O.A.; Niemantsverdriet, J.W. Electrocatalysts for the generation of hydrogen, oxygen and synthesis gas. *Prog. Energy Combust. Sci.* **2017**, *58*, 1–35. [CrossRef]
32. Yang, H.; Chen, Z.; Guo, P.; Fei, B.; Wu, R. B-doping-induced amorphization of LDH for large-current-density hydrogen evolution reaction. *Appl. Catal. B-Environ.* **2020**, *261*, 118240. [CrossRef]
33. Wang, D.; Li, J.; Zhao, Y.; Xu, H.; Zhao, J. Bifunctional Cu_2Se-$Co(OH)_2$ nanotube array/Cu foam electrocatalyst for overall water splitting. *Electrochim. Acta* **2019**, *316*, 8–18. [CrossRef]
34. Wang, Z.; Ji, S.; Liu, F.; Wang, H.; Wang, X.; Wang, Q.; Pollet, B.G.; Wang, R. Highly Efficient and Stable Catalyst Based on $Co(OH)_2$@Ni Electroplated on Cu-Metallized Cotton Textile for Water Splitting. *ACS Appl. Mater. Interfaces* **2019**, *11*, 29791–29798. [CrossRef] [PubMed]
35. Geng, B.; Yan, F.; Liu, L.; Zhu, C.; Li, B.; Chen, Y. Ni/MoC heteronanoparticles encapsulated within nitrogen-doped carbon nanotube arrays as highly efficient self-supported electrodes for overall water splitting. *Chem. Eng. J.* **2021**, *406*, 126815. [CrossRef]
36. Han, X.; Wu, X.; Deng, Y.; Liu, J.; Lu, J.; Zhong, C.; Hu, W. Ultrafine Pt Nanoparticle-Decorated Pyrite-Type CoS_2 Nanosheet Arrays Coated on Carbon Cloth as a Bifunctional Electrode for Overall Water Splitting. *Adv. Energy Mater.* **2018**, *8*, 1800935. [CrossRef]
37. Koutauarapu, R.; Reddy, C.V.; Babu, B.; Reddy, K.R.; Cho, M.; Shim, J. Carbon cloth/transition metals-based hybrids with controllable architectures for electrocatalytic hydrogen evolution-A review. *Int. J. Hydrogen Energy* **2020**, *45*, 7716–7740. [CrossRef]
38. Zhang, Q.; Xiao, W.; Guo, W.; Yang, Y.; Lei, J.; Luo, H.; Li, N. Macroporous Array Induced Multiscale Modulation at the Surface/Interface of $Co(OH)_2$/NiMo Self–Supporting Electrode for Effective Overall Water Splitting. *Adv. Funct. Mater.* **2021**, *31*, 2102117. [CrossRef]
39. Cheng, C.; Liu, F.; Zhong, D.; Hao, G.; Liu, G.; Li, J.; Zhao, Q. Three-dimensional self-supporting catalyst with NiFe alloy/oxyhydroxide supported on high-surface cobalt hydroxide nanosheet array for overall water splitting. *J. Colloid Interface Sci.* **2022**, *606*, 873–883. [CrossRef]
40. Gu, L.-F.; Li, C.-F.; Zhao, J.-W.; Xie, L.-J.; Wu, J.-Q.; Ren, Q.; Li, G. Dual modulation of lattice strain and charge polarization induced by $Co(OH)_2$/$Ni(OH)_2$ interfaces for efficient oxygen evolution catalysis. *J. Mater. Chem. A* **2021**, *9*, 13279–13287. [CrossRef]
41. Song, Z.; Han, X.; Deng, Y.; Zhao, N.; Hu, W.; Zhong, C. Clarifying the Controversial Catalytic Performance of $Co(OH)_2$ and Co_3O_4 for Oxygen Reduction/Evolution Reactions toward Efficient Zn-Air Batteries. *ACS Appl. Mater. Interfaces* **2017**, *9*, 22694–22703. [CrossRef] [PubMed]
42. Dileep, N.P.; Vineesh, T.V.; Sarma, P.V.; Chalil, M.V.; Prasad, C.S.; Shaijumon, M.M. Electrochemically Exfoliated β-$Co(OH)_2$ Nanostructures for Enhanced Oxygen Evolution Electrocatalysis. *ACS Appl. Energy Mater.* **2020**, *3*, 1461–1467. [CrossRef]
43. Guo, D.; Luo, Y.; Yu, X.; Li, Q.; Wang, T. High performance $NiMoO_4$ nanowires supported on carbon cloth as advanced electrodes for symmetric supercapacitors. *Nano Energy* **2014**, *8*, 174–182. [CrossRef]
44. SRay, K.; Dhakal, D.; Regmi, C.; Yamaguchui, T.; Lee, S.W. Inactivation of Staphylococcus aureus in visible light by morphology tuned α-$NiMoO_4$. *J. Photochem. Photobiol. A Chem.* **2018**, *350*, 59–68.
45. Wang, A.-L.; Xu, H.; Li, G.-R. NiCoFe Layered Triple Hydroxides with Porous Structures as High-Performance Electrocatalysts for Overall Water Splitting. *ACS Energy Lett.* **2016**, *1*, 445–453. [CrossRef]
46. Huang, M.; Liu, W.; Wang, L.; Liu, J.; Chen, G.; You, W.; Zhang, J.; Yuan, L.; Zhang, X.; Che, R. Self-transforming ultrathin α-$Co(OH)_2$ nanosheet arrays from metal-organic framework modified graphene oxide with sandwichlike structure for efficient electrocatalytic oxygen evolution. *Nano Res.* **2020**, *13*, 810–817. [CrossRef]
47. Peng, S.; Li, L.; Wu, H.B.; Madhavi, S.; Lou, X.W. Controlled Growth of $NiMoO_4$ Nanosheet and Nanorod Arrays on Various Conductive Substrates as Advanced Electrodes for Asymmetric Supercapacitors. *Adv. Energy Mater.* **2015**, *5*, 1401172. [CrossRef]

48. Ray, S.K.; Dhakal, D.; Sohng, J.K.; Kim, S.-Y.; Lee, S.W. Efficient inactivation of Pseudomonas aeruginosa by Cu/Co-α-$NiMoO_4$ in visible light. *Chem. Eng. J.* **2018**, *347*, 366–378. [CrossRef]
49. Karmakar, A.; Karthick, K.; Sankar, S.S.; Kumaravel, S.; Ragunath, M.; Kundu, S. Oxygen vacancy enriched $NiMoO_4$ nanorods via microwave heating: A promising highly stable electrocatalyst for total water splitting. *J. Mater. Chem. A* **2021**, *9*, 11691–11704. [CrossRef]
50. Xu, C.; Lu, W.; Yan, L.; Ning, J.; Zheng, C.; Zhong, Y.; Zhang, Z.; Hu, Y. Hierarchical molybdenum-doped cobaltous hydroxide nanotubes assembled by cross-linked porous nanosheets with efficient electronic modulation toward overall water splitting. *J. Colloid Interface Sci.* **2020**, *562*, 400–408. [CrossRef]
51. Xu, L.; Jiang, Q.; Xiao, Z.; Li, X.; Huo, J.; Wang, S.; Dai, L. Plasma-Engraved Co3O4 Nanosheets with Oxygen Vacancies and High Surface Area for the Oxygen Evolution Reaction. *Angew. Chem.-Int. Ed.* **2016**, *55*, 5277–5281. [CrossRef] [PubMed]
52. Sung, M.-C.; Lee, G.-H.; Kim, D.-W. $CeO_2/Co(OH)_2$ hybrid electrocatalysts for efficient hydrogen and oxygen evolution reaction. *J. Alloys Compd.* **2019**, *800*, 450–455. [CrossRef]
53. Sriram, S.; Mathi, S.; Vishnu, B.; Jayabharathi, J. Entwined $Co(OH)_2$ In Situ Anchoring on 3D Nickel Foam with Phenomenal Bifunctional Activity in Overall Water Splitting. *Energy Fuels* **2022**, *36*, 7006–7016. [CrossRef]
54. Wang, Y.; Yang, Y.; Wang, X.; Li, P.; Shao, H.; Li, T.; Liu, H.; Zheng, Q.; Hu, J.; Duan, L.; et al. Electro-synthesized $Co(OH)_2$@CoSe with Co-OH active sites for overall water splitting electrocatalysis. *Nanoscale Adv.* **2020**, *2*, 792–797. [CrossRef]
55. Zhang, X.; Su, H.; Du, X. A nickel molybdenum oxide nanoarray as an efficient and stable electrocatalyst for overall water splitting. *New J. Chem.* **2020**, *44*, 8176–8182. [CrossRef]
56. Chen, L.; Deng, Z.; Chen, Z.; Wang, X. Building Ni_9S_8/MoS_2 Nanosheets Decorated $NiMoO_4$. Nanorods Heterostructure for Enhanced Water Splitting. *Adv. Mater. Interfaces* **2021**, *8*, 2101483. [CrossRef]
57. Cho, Y.; Lee, J.; Nguyen, T.T.-H.; Bae, J.W.; Yu, T.; Lim, B. Facile synthesis of flower-like α-$Co(OH)_2$ nanostructures for electrochemical water splitting and pseudocapacitor applications. *J. Ind. Eng. Chem.* **2016**, *37*, 175–179. [CrossRef]
58. Luo, Y.; Gong, M.; Wang, J.; Zhao, P.; Yang, X.; Cui, S.; Li, Z.; Jiao, Z.; Cheng, L. Preparation of $NiMoO_4$ nanoarrays electrodes with optimized morphology and internal crystal water for efficient supercapacitors and water splitting. *Colloids Surf. A Physicochem. Eng. Asp.* **2022**, *655*, 130119. [CrossRef]
59. Li, Y.; Sun, Y.; Qin, Y.; Zhang, W.; Wang, L.; Luo, M.; Yang, H.; Guo, S. Recent Advances on Water-Splitting Electrocatalysis Mediated by Noble-Metal-Based Nanostructured Materials. *Adv. Energy Mater.* **2020**, *10*, 1903120. [CrossRef]
60. Xu, Y.; Kraft, M.; Xu, R. Metal-free carbonaceous electrocatalysts and photocatalysts for water splitting. *Chem. Soc. Rev.* **2016**, *45*, 3039–3052. [CrossRef]
61. Zhang, J.; Zhang, Q.; Feng, X. Support and Interface Effects in Water-Splitting Electrocatalysts. *Adv. Mater.* **2019**, *31*, 1808167. [CrossRef] [PubMed]